Catalysis Science & Technology

ROYAL SOCIETY OF CHEMISTRY

PAPER

View Article Online
View Journal | View Issue



Cite this: *Catal. Sci. Technol.*, 2020, **10**, 187

# Theoretically predicted surface morphology of FCC cobalt nanoparticles induced by Ru promoter†

Lili Liu,[ab] Mengting Yu,[ab] Qiang Wang,*[a] Bo Hou,[a] Litao Jia,[ac] Congbiao Chen[a] and Debao Li*[ac]

Received 19th September 2019,
Accepted 13th November 2019

DOI: 10.1039/c9cy01892a

rsc.li/catalysis

The experimental shape control of metallic Co nanoparticles (NPs) remains a great challenge in terms of their direct characterization for the further rational design and optimization of efficient nanocatalysts nowadays, especially when a low promoter content is involved. Thus, spin-polarized density functional theory (DFT) and *ab initio* molecular dynamics (AIMD) simulations have been carried out to investigate the adsorption configurations and growth trend of $Ru_n$ clusters on Co surfaces to systemically explore the surface morphology of Co NPs induced by Ru promotion in Co-based Fischer–Tropsch synthesis (FTS). The predicted $Ru_n$ aggregation adsorption patterns on Co(100) and Co(110) surfaces combined with the recent results for Co(111) and Co(311) surfaces show the thermodynamic growth tendency that $Ru_n$ aggregates are favorable for planar layered growth on Co surfaces under realistic FTS reaction conditions, which is consistent with the experimental EELS spectral results. The addition of Ru promoter has an important role in tuning the stability of the exposed facets of face-centered-cubic (FCC) Co NPs, accompanied by the change from truncated octahedron to rhombic dodecahedron morphology. At high Ru content, the increased high index Co(311) and Co(110) surfaces, including more active step and kink sites, are desirable for the enhanced activity of FCC Co NPs.



## 1. Introduction

With the increasing demand for and limited availability of petroleum resources, alternative and sustainable routes starting with synthesis gas (CO + $H_2$) derived from coal, natural gas, or biomass to produce chemicals and fuels are more desirable.[1,2] The typical process based on synthesis gas is Fischer–Tropsch synthesis (FTS),[3–5] a heterogeneous catalytic technique for the production of clean transportation fuels and various hydrocarbons by different catalysts.[6–9] Co-based catalysts are promising for long-chain hydrocarbons and distinguished from other FTS catalysts by higher intrinsic activity, higher selectivity towards paraffin, higher resistance toward deactivation and lower activity for the competing water gas shift reaction.[10–13] Cobalt catalysts for industrial applications usually contain not only catalytically active cobalt and supports, but also small amounts of promoters to improve the activity, selectivity, and stability of the catalysts.[14–17]

Modification of catalysts with promoters, especially noble metals, shows great promise to attain optimum catalytic performance through changing the structure, size and dispersion or modifying the electronic characters of the active phase.[18–20] Extensive studies, including detailed characterization, have suggested that enhanced Co reducibility and higher selectivity for heavier ($C_{5+}$) hydrocarbons could be achieved by adding ruthenium promoter to cobalt catalysts.[21–23] Balakrishnan *et al.* found that Ru promoted Co catalysts exhibit higher catalytic stability because the Ru inhibits the C–C coupling reaction and prevents the deposition and growth of C species on the catalyst surface.[24] The addition of Ru can also shift the temperature required to reduce cobalt oxide to the metallic state to a significantly lower temperature, resulting in a higher Co site density during FTS catalysis.[25,26] In contrast to the decreased TOF by the introduction of Pd and Pt, the turnover frequency (TOF) based on a Ru modified Co surface evaluated by $H_2$ uptake is increased to some extent, owing to the increased bridge-type adsorption of CO facilitating the dissociation of CO into carbon and oxygen.[27]

Several groups of researchers have been devoted to investigating the location and distribution of the Ru

[a] *State Key Laboratory of Coal Conversion, Institute of Coal Chemistry, Chinese Academy of Sciences, No.27 South Taoyuan Road, Taiyuan, Shanxi 030001, People's Republic of China. E-mail: wqiang@sxicc.ac.cn, dbli@sxicc.ac.cn*
[b] *University of Chinese Academy of Sciences, Beijing 100049, People's Republic of China*
[c] *Dalian National Laboratory for Clean Energy, Dalian, 116023, China*

† Electronic supplementary information (ESI) available. See DOI: 10.1039/c9cy01892a

promoter in reduced cobalt catalysts, aiming to unveil the significant functioning mechanisms of the involvement of Ru promotion and the interaction of Co and Ru in FTS reaction. The experimental results obtained with Ru, Re, Pt, and Ir promoters as reduction promoters revealed that the majority of the promoter introduced by co-impregnation with cobalt remains monometallic particles located in the microscopic structure of the cobalt catalysts.[23,28–30] Iglesia *et al.* disclosed the formation of intermetallic particles rather than CoRu alloy during the precursor solution reduction process.[31,32] They believed that Ru promoter added in a separate second step of the oxidation–reduction procedures would lead to separate Co and Ru phases and a large fraction of the Ru remaining exposed near the outer crystallite surfaces after calcination. This was demonstrated subsequently by Ru K-edge EXAFS radial distribution functions with Ru as the reduction promoter by Kungurova *et al.*[33] A recent report has concluded that the Ru aggregates precipitated as individual atoms or as small clusters on the surface of the Co NPs after a two-step reduction process of Co precursors.[34]

Although the promotion role and the location of Ru in Co-based catalysts has been recognized, such surface structures of Ru promoters on metallic Co and the morphology of Co NPs decorated by Ru promoter still represent a great challenge for direct characterization, even if Ru was identified in patches on Co particles by EELS spectrum imaging by Shannon *et al.*[35] Since it is experimentally difficult to study the properties of individual NPs at the atomic level, theoretical approaches are highly suitable to provide information about the structure and morphology of NPs.[36,37] Many excellent theoretical studies have been successfully conducted concerning the equilibrium morphology of metal NPs in reaction conditions, such as: metallic Fe and iron carbide promoted by $K_2O$,[38,39] Cu NPs supported by ZnO,[36] Pt NPs etched by HCl,[40] Ru NPs under a hydrogen atmosphere,[41] and Pd, Pt, and Rh NPs under NO and CO gas environments.[42] However, there is no systematic investigation offering atomic information regarding the structures of Ru promoters on Co NPs. The stabilized effect of the Ru promoter on the morphology of Co NPs was also generally neglected in previous experimental studies.[43] Therefore, it is necessary to apply a theoretical model to predict the morphology evolution of Co NPs induced by Ru promoter.

In this work, we investigated the structures and adsorption pattern of $Ru_n$ clusters on Co(100) and Co(110) surfaces based on spin-polarized density functional theory calculations and *ab initio* molecular dynamics simulations, and combined with those recently reported results on Co(111) and Co(311) surfaces,[44] with the aim of further systematically determining the morphology evolution of face-centered-cubic (FCC) Co NPs stabilized by Ru promoter. The elucidation of the facet-dependent equilibrium morphology of Ru-promoted metallic Co NPs is expected to provide useful guidance for advanced experimental characterization, which is important for understanding the effect of Ru promoter in Co-based FTS.

## 2. Computational details

### 2.1 Models

FCC crystalline cobalt was chosen as the model in view of its excellent stability and FTS activity with a diameter <20 nm. The determined equilibrium lattice constant of FCC Co is 3.53 Å, which is consistent with the experimental result[45] (3.55 Å) and theoretical value (3.52 Å,[46] 3.54 Å[47]). The Co surface was modeled by periodic slabs consisting of four layers in the (100) surface and six layers in the (110) surface, with $p(4 \times 4)$ and $p(3 \times 4)$ supercells in lateral directions, respectively. The optimized structures of Co(100) and Co(110) surfaces as well as the possible adsorption sites are shown in Fig. S1.† During the computational process, the Ru atoms and upper two atomic layers were relaxed without any symmetry or direction restrictions to optimize the surface structure, while the remaining atoms were frozen to simulate the bulk structure for the description of $Ru_n$ adsorption on Co surfaces. The Brillouin zone integration was achieved by summation over specially selected *k*-points using the Monkhorst-Pack scheme,[48] where $(9 \times 9 \times 9)$ and $(3 \times 3 \times 1)$ *k*-point meshes were chosen for bulk and Co surfaces, respectively. The vacuum region of 15 Å was applied to prevent interactions between the periodically repeating slabs.

### 2.2 Methods

All the static calculations were carried out by spin-polarized density functional theory (DFT) implemented in the Vienna *Ab Initio* Simulation Package (VASP).[49,50] The exchange correlation energy of the electrons was treated within the generalized gradient approximation (GGA) with the Perdew–Burke–Ernzerh (PBE) of exchange–correlation functional.[51] The interactions between ion cores and valence electrons were described by the projector augmented wave (PAW) method.[52,53] The solution of the Kohn–Sham equations was expanded in a plane-wave basis set with a cutoff energy of 400 eV. Final convergence criteria for the energy and Hellmann–Feynman forces were $10^{-5}$ eV and 0.03 eV $Å^{-1}$, respectively. Bader charge analysis[54,55] was carried out to obtain the effective charge of different atoms in the $Ru_n$ adsorption system. The location and energy of transition states (TSs) of the Ru atom diffusion were determined with the climbing image nudged elastic band (CI-NEB) method,[56] and the vibrational frequencies were analyzed to confirm the transition state with only one imaginary frequency. In addition, *ab initio* molecular dynamics (AIMD) simulations were performed to probe the growth trend of the Ru nanoclusters on the Co surfaces within the NVT canonical ensemble. A detailed description of the AIMD simulations is available in the literature.[44]

 

# 3. Results and discussion

### 3.1 Morphology and surface stability of pure FCC Co NPs

The pure FCC Co unit cell adopts a space point group of $O_h$ with high symmetry. The equilibrium shape and relative surface distribution of FCC Co were obtained by Wulff construction based on the bulk symmetries and calculated surface energies. As shown in Fig. 1, FCC Co exhibits a regular truncated octahedron shape and contains four different facets. It is covered predominantly with eight close-packed (111) facets, accounting for about 72.4% of the total surface area. The remaining three exposed facts, (100), (311) and (110), cover relatively smaller fractions of surface area, namely, 13.9%, 8.9%, and 4.8%, respectively. The stability order of the exposed facets follows the ascending order: Co(110) < Co(311) < Co(100) < Co(111) with surface energies of 0.161, 0.158, 0.157 and 0.132 eV Å$^{-2}$, respectively, where Co(111) is the most stable surface and Co(311) is the least stable surface. It is worth noting that the metal-promoters interaction under operating conditions might affect the corresponding morphology, stability and reactivity of exposed crystallographic facets. Therefore, it is necessary to explore the effect of Ru promoter on the structure and morphology of Co NPs in real FTS conditions.

### 3.2 Structure and adsorption pattern of Ru$_n$ clusters on FCC Co

The investigation of the Ru$_n$ adsorption on Co(100) and Co(110) surfaces combined with previous studies on the Co(111) and Co(311) surfaces[44] is expected to build a comprehensive understanding of the morphology of Ru-promoted Co NPs. For Ru$_n$ adsorption on Co surfaces, both two-dimensional monolayer structures and three-dimensional structures with partial Ru atoms deposited on Co surfaces were examined. Possible initial structures for Ru$_n$ cluster adsorption on Co surfaces at different coverages were constructed and optimized to find the most preferred Ru$_n$ adsorption pattern, as presented in Fig. S2 and S3.† The most stable adsorption configurations of Ru$_n$ ($n$ = 1–8) clusters on Co(100) and Co(110) surfaces are shown in Fig. 2 and 3, and the energetic results along with the structural information are listed in Tables 1 and 2.

**3.2.1 Adsorption pattern of Ru$_n$ on Co(100) and Co(110) surfaces.** The lowest energy adsorption of a single Ru atom on Co(100) surface is that on the four-fold (4F) site. Such energetic preference for Ru adsorption is also found at higher coverage. With the increase in Ru$_n$ ($n$ = 1–4) cluster size, a linear structure of Ru$_4$-a and a square structure of Ru$_4$-b with the same thermodynamic preferences are formed. On further addition of Ru atoms, the resultant Ru$_n$ ($n$ = 5–6) configurations with linear-based and square-based structures both have the newly added Ru atom adsorbed at the 4F site and interacting with the neighboring Ru$_4$ unit to form a branched structure due to periodicity. On the basis of Ru$_6$ adsorption, the most stable Ru$_n$ ($n$ = 7–8) adsorption configurations with an ordered-square structure were obtained. For the adsorption of the Ru$_n$ clusters on a Co(100) surface, both line-based and square-based adsorption patterns are available because of their close adsorption energies. Despite their obvious differences in the structure at low coverage, the two adsorption patterns are bound to merge into a periodic square-based row structure limited by the boundary conditions, which is expected for subsequent monolayer adsorption.

The adsorption pattern of Ru$_n$ on Co(110) surface is quite different from that on Co(100) surface owing to its corrugated surface structure. A single Ru atom favors adsorbing at the five-fold (5F) site at the corrugated bottom on Co(110) surface. Further addition of Ru atoms to the 5F site prior to other sites was confirmed. For the adsorption of Ru$_n$ ($n$ = 1–4), the newly added Ru atoms of the most stable adsorption configuration are adsorbed with direct Ru–Ru interactions along the corrugated direction, gradually forming a linear chain on Co(110) surface. On further addition of Ru atoms, due to the limitation of surface size, the most stable aggregated Ru$_n$ clusters ($n$ = 5–8) become another parallel independent chain with all of the Ru atoms adsorbed at the 5F sites. The most stable adsorption configuration Ru$_8$ is the double-chained structure, which can be regarded as the combination of two Ru$_4$ structures. Therefore, it can be inferred that the initial adsorption of the Ru atoms on Co(110) surface is in the line-band-layer pattern and a monolayer Ru covered surface can be expected at high coverage.

The two-dimensional dispersed configurations were also investigated for the Ru$_n$ adsorption on Co(100) and Co(110) surfaces, higher in energy than that of the aggregated configurations, indicating the strong aggregation ability of Ru atoms. In addition, the three-dimensional clusters are found to be energetically less stable than the most stable two-dimensional isomers, owing to their higher surface energies caused by the more edge and vertex atoms. To verify this conclusion, the possible structures and energies of the large Ru$_{11}$ clusters were calculated. The most stable Ru$_{11}$ adsorption configurations on Co(100) and Co(110) surfaces are presented in Fig. S4 and S5† and are found to be in line with the above obtained adsorption mechanism.

**3.2.2 Energy analysis of FCC Co surfaces.** The larger average adsorption energies and stepwise adsorption energies of Ru$_n$ clusters than those of atomic Ru reveal that the formation of Ru clusters is energetically favored on the Co

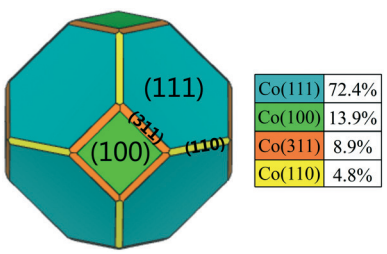


Fig. 1 The equilibrium shape of pure FCC Co NPs obtained by Wulff construction.

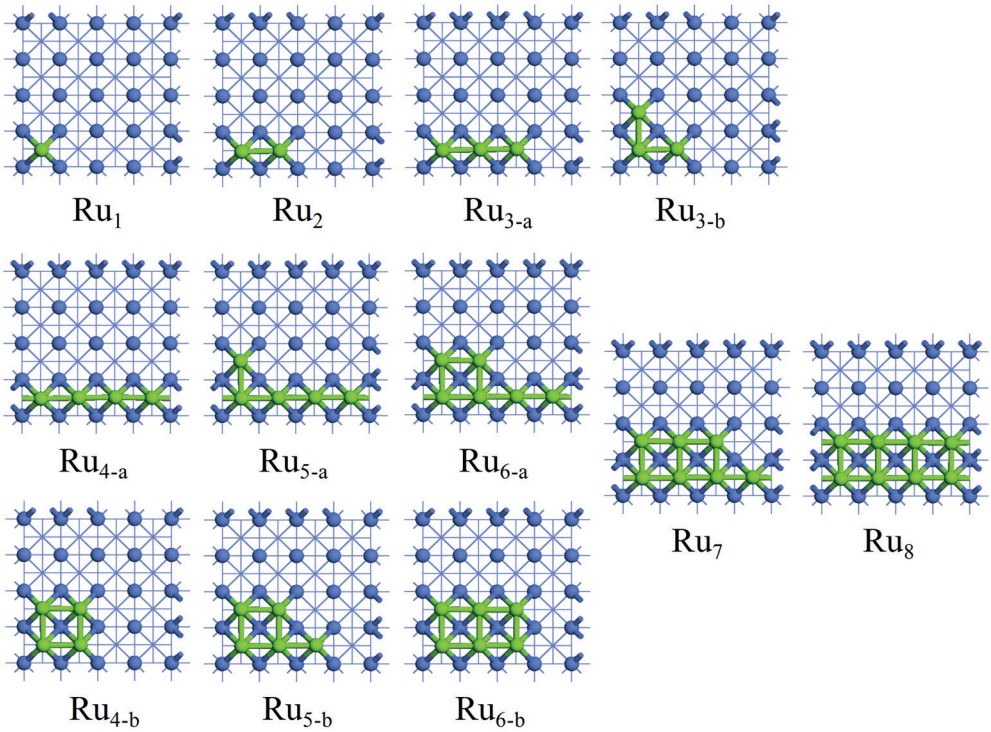


**Fig. 2** The stable adsorption configurations of $Ru_n$ ($n$ = 1–8) on Co(100) surface. The Co and Ru atoms are shown as blue and light green spheres, respectively.

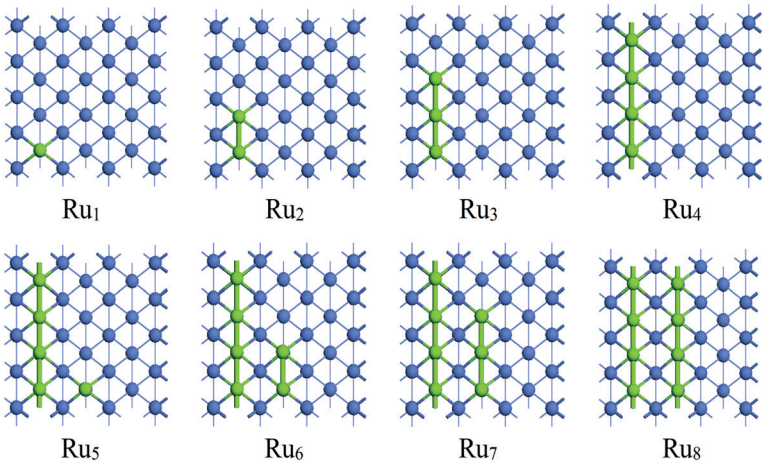


**Fig. 3** The stable adsorption configurations of $Ru_n$ ($n$ = 1–8) on Co(110) surface. The Co and Ru atoms are shown as blue and light green spheres, respectively.

surfaces. The obvious difference of adsorption energies between different Co surfaces clearly reveals strong surface structure sensitivity for the $Ru_n$ adsorption. For the $Ru_n$ clusters with equal size, the strongest adsorption was found on the Co(311) surface, followed by the Co(110) and Co(100) surfaces, while the adsorption on Co(111) surface was the weakest. These results can be attributed to the differences in the coordination number of Ru adsorbed on Co surfaces.

Generally, the Co–Ru interaction affected by the distinct Co surface structures is reflected in the hybrid d orbitals between the Co and Ru, as shown in Fig. S6.† The projected d orbitals of the Co(100) and Co(110) surfaces shifted towards a lower energy after $Ru_n$ adsorption, leading to the electronic loss of Co surfaces. In addition, there is a stronger d-orbital mixing near the Fermi level between the adsorbed $Ru_{11}$ cluster on Co(110) surface than on Co(100) surface, implying the stronger binding strength between the Co(110) surface and the $Ru_{11}$ cluster, coinciding with the trend of adsorption energies. The results of the electronic properties analysis suggest that compared with the flat Co(111) and

 

**Table 1** Various energies ($E$, eV), average Ru–Ru distances ($d_{Ru-Ru}$, Å) and average Bader charge ($q$, e) for $Ru_n$ ($n$ = 1–8) on Co(100) surface

| $Ru_n$ | $E(Ru_{n/ads})$ | $E(Ru_{ads/av})$ | $\Delta E(Ru_{ads})$ | $E_{agg}$ | $E_{growth}$ | $E_{int}(Ru_{ads})$ | $E_{int}$(Ru–Co) | $E_{int/av}$(Ru–Co) | $d_{Ru-Ru}$ | $q$ |
|---|---|---|---|---|---|---|---|---|---|---|
| $Ru_1$ | −5.26 | −5.26 | −5.26 | | | | −6.45 | −6.45 | | −0.18 |
| Line-based adsorption pattern | | | | | | | | | | |
| $Ru_2$-a/b | −10.76 | −5.38 | −5.51 | −0.12 | −0.25 | −0.25 | −7.29 | −3.65 | 2.57 | −0.19 |
| $Ru_3$-a | −16.51 | −5.50 | −5.74 | −0.25 | −0.49 | −0.74 | −12.17 | −4.06 | 2.53 | −0.21 |
| $Ru_4$-a | −22.76 | −5.69 | −6.25 | −0.43 | −0.99 | −1.73 | −14.10 | −3.53 | 2.51 | −0.18 |
| $Ru_5$-a | −28.46 | −5.69 | −5.70 | −0.44 | −0.45 | −2.18 | −16.26 | −3.25 | 2.51 | −0.16 |
| $Ru_6$-a | −34.96 | −5.83 | −6.50 | −0.57 | −1.24 | −3.42 | −16.92 | −2.82 | 2.46 | −0.14 |
| Square-based adsorption pattern | | | | | | | | | | |
| $Ru_3$-b | −16.40 | −5.47 | −5.63 | −0.21 | −0.38 | −0.63 | −10.94 | −3.65 | 2.52 | −0.15 |
| $Ru_4$-b | −22.92 | −5.73 | −6.52 | −0.47 | −1.26 | −1.89 | −11.56 | −2.89 | 2.41 | −0.10 |
| $Ru_5$-b | −28.64 | −5.73 | −5.72 | −0.47 | −0.47 | −2.36 | −15.04 | −3.01 | 2.46 | −0.11 |
| $Ru_6$-b | −34.91 | −5.82 | −6.27 | −0.56 | −1.00 | −3.36 | −16.76 | −2.79 | 2.47 | −0.11 |
| $Ru_7$-a/b | −41.27 | −5.90 | −6.36 | −0.64 | −1.11 | −4.47 | −19.10 | −2.73 | 2.48 | −0.13 |
| $Ru_8$-a/b | −48.16 | −6.02 | −6.89 | −0.76 | −1.63 | −6.11 | −19.64 | −2.46 | 2.47 | −0.12 |
| 3D structures | | | | | | | | | | |
| $Ru_5$-c | −28.16 | −5.63 | | −0.38 | | −1.88 | −12.02 | −2.40 | 2.49 | −0.07 |
| $Ru_6$-c | −33.98 | −5.66 | | −0.41 | | −2.44 | −15.20 | −2.53 | 2.50 | −0.07 |
| $Ru_7$-c | −40.40 | −5.77 | | −0.52 | | −3.61 | −17.48 | −2.50 | 2.50 | −0.09 |
| $Ru_8$-c | −46.79 | −6.68 | | −0.59 | | −4.74 | −19.17 | −2.40 | 2.51 | −0.10 |

**Table 2** Various energies ($E$, eV), average Ru–Ru distances ($d_{Ru-Ru}$, Å) and average Bader charge ($q$, e) for $Ru_n$ ($n$ = 1–8) on Co(110) surface

| $Ru_n$ | $E(Ru_{n/ads})$ | $E(Ru_{ads/av})$ | $\Delta E(Ru_{ads})$ | $E_{agg}$ | $E_{growth}$ | $E_{int}(Ru_{ads})$ | $E_{int}$(Ru–Co) | $E_{int/av}$(Ru–Co) | $d_{Ru-Ru}$ | $q$ |
|---|---|---|---|---|---|---|---|---|---|---|
| $Ru_2$ | −11.45 | −5.72 | −6.03 | −0.31 | −0.62 | −6.39 | −8.46 | −4.23 | 2.52 | −0.17 |
| $Ru_3$ | −17.56 | −5.85 | −6.11 | −0.44 | −0.69 | −9.97 | −12.98 | −4.33 | 2.50 | −0.18 |
| $Ru_4$ | −24.47 | −6.12 | −6.91 | −0.70 | −1.50 | −14.36 | −15.71 | −3.93 | 2.50 | −0.20 |
| $Ru_5$ | −29.89 | −5.98 | −5.42 | −0.56 | −0.01 | −17.26 | −20.40 | −4.08 | 2.49 | −0.17 |
| $Ru_6$ | −35.98 | −6.00 | −6.09 | −0.58 | −0.68 | −20.82 | −22.43 | −3.74 | 2.49 | −0.15 |
| $Ru_7$ | −42.11 | −6.02 | −6.13 | −0.60 | −0.71 | −24.42 | −26.28 | −3.68 | 2.50 | −0.14 |
| $Ru_8$ | −48.90 | −6.11 | −6.79 | −0.70 | −1.37 | −28.68 | −28.33 | −3.54 | 2.50 | −0.16 |

Co(100) surfaces, the corrugated Co(311) and Co(110) surfaces have stronger Ru/Co interaction, accompanied by more electron transfer, which conforms to the trend of adsorption energy.

It can be obtained from the data of Tables S1 and S2† that Co(110) surface has the strongest affinity and aggregation potential of $Ru_n$ at low coverage, while the affinity of the Co(100) surface becomes stronger and the aggregation potential of Co(111) surface becomes higher as the $Ru_n$ size increases. Based on the results of the calculated interaction energies, it is found that the Ru–Ru interaction increases while the average Ru–Ru bond gradually decreases as the $Ru_n$ cluster becomes larger, indicating that the increased stability is accompanied by the increased $Ru_n$ cluster size. Although the interaction energy between each Ru adatom and both Co surfaces decreases, the total interaction energy between the $Ru_n$ cluster and both Co surfaces increases with increasing adsorbed Ru atoms. Therefore, the bonding of $Ru_n$ clusters and Co surfaces is enhanced. In addition, the value of growth energies of the $Ru_n$ clusters adsorbed on Co surfaces decreases with the increase in size of the $Ru_n$ cluster. Growth of $Ru_n$ clusters on Co surfaces is thermodynamically favorable and exothermic. With the $Ru_n$ cluster size increasing, the growth characteristics of the $Ru_n$ clusters on Co surfaces appear to be significantly different. It is worth noting that there is a local minimum in the decreasing stepwise adsorption energies and growth energies when the $Ru_n$ clusters size increases to $Ru_4$ among all adsorption configurations on the Co surfaces, indicating that $Ru_4$ is the critical size of growth of $Ru_n$ clusters.

Consequently, it is believed that the two-dimensional aggregation structures are favored on Co surfaces and this thermodynamic preference can be expected to give monolayer growth. The obtained aggregation properties of $Ru_n$ clusters agree well with the previous experiment results,[35] where the Ru promoter is present in islands on Co particles at a thickness of one monolayer or at most two monolayers.

**3.2.3 Diffusion of a single Ru atom.** The aggregation potential of $Ru_n$ can also be evaluated from the diffusion barrier of a single Ru atom on Co surfaces.[35,57] As shown in Fig. S7,† the migration of a single Ru atom on a Co(100) surface from one 4F site to the adjacent 4F site (*via* P) needs a moderate energy barrier of 0.79 eV. For Co(110) surface, the diffusion barrier of a Ru atom from one 5F site to the adjacent 5F site along the chain growth direction (*via* P1) is only 0.23 eV, while across the corrugated direction (*via* P2), the migration of a Ru atom to the parallel 5F site must overcome a minimum of 1.64 eV barrier. These small

diffusion barriers show that an adsorbed Ru atom may diffuse easily and bond with other Ru atoms or clusters that are already deposited on the Co surface, thus contributing to the $Ru_n$ cluster aggregation and formation. These results are in agreement with the $Ru_n$ adsorption patterns on Co(100) and Co(110) surfaces proposed above. Compared with our previous investigated results,[44] the weak adsorption can make Ru migration easier, and the mobility of a single Ru atom follows the order: Co(111) > Co(110) > Co(311) > Co(100), where the lowest diffusion energy on Co(111) surface corresponds to the weakest adsorption.

**3.2.4 AIMD simulations.** To elucidate the preferential growth trend of Ru promoters deposited on Co surfaces under a realistic catalytic environment, AIMD simulations were performed at 1000 K to illustrate the structural evolution of adsorbed $Ru_{11}$ clusters. The elevated temperature compared to the practical reduced condition of 673–723 K[58–61] in cobalt-based FTS was used to accelerate sampling to the low-energy-barrier events. The initial configuration is shown in Fig. 4, where the most stable three-dimensional $Ru_{11}$ cluster[62] in the gas phase was deposited at the energetically favorable position of Co substrates simulated by the slab models of Co(100) with $p(6 \times 4)$ and Co(110) with $p(5 \times 4)$ to accommodate the fluctuating cluster. The bottom two layers of the slab were frozen, and the remaining atoms were allowed to relax in optimization.

The trajectories of the $Ru_{11}$ structure evolution on Co(100) and Co(110) surfaces from AIMD simulations are displayed in Video S1 and S2.† Not surprisingly, the supported $Ru_{11}$ cluster undergoes restructuring rapidly and reaches the final equilibrium structures (shown in Fig. 4) after 10 ps: a square-based row structure of $Ru_{11}$ on the Co(100) surface and a parallel independent chain structure of $Ru_{11}$ on the Co(110) surface, similar to the energetically most favorable $Ru_{11}$ configurations from DFT calculation. These results indicate

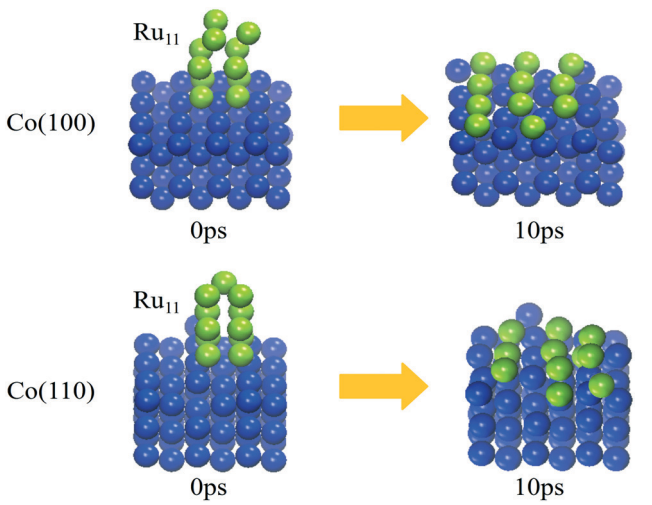


Fig. 4 The image of the initial and final structures at 10 ps of the $Ru_{11}$ cluster deposited on the Co(100) and (110) surfaces from the AIMD simulations. The blue and light green balls represent Co atoms and Ru atoms, respectively.

that the Ru atoms in the upper layers are inclined to migrate to the Co surfaces with more Co–Ru bonds, similar to that of Co(111) and Co(311) surfaces. Thus, this phenomenon can serve as direct evidence for Ru clusters preferring two dimensional aggregation structures on FCC Co surfaces under realistic cobalt-based FTS reaction conditions, consistent with the experimental results[35] by EELS spectrum imaging that Ru was associated with cobalt particles in patches at a thickness of one monolayer or at most two monolayers.

### 3.3 Morphology of FCC Co NPs induced by Ru promoter

Based on the preferential Ru adsorption pattern, the growth energies with respect to the size of $Ru_n$ clusters on FCC Co surfaces were investigated. As shown in Fig. S8,† the $Ru_4$ cluster has the highest growth energy during the growth of Ru clusters to form periodic structures, indicating that a $Ru_4$ cluster is most likely to exist on the Co surfaces. Surface energy determines the crystallite morphology of FCC Co and is considered to be an important index for evaluating the relative stability of active surfaces. The most stable structural unit of $Ru_4$ with the greatest probability is subsequently used to calculate the surface energy of each surface with different Ru content.

According to the definition of surface energy, the lower the surface energy is, the more stable the surface structure is. The surface energies of Co surfaces modified by Ru at different Ru/Co atomic ratios are listed in Table 3. It is found that the surface energies can be tuned by Ru content. As the surface Ru/Co atomic ratio increases, all surface energies decrease, meaning that the stability of all facets upon Ru adsorption can be enhanced significantly. From the variation curves in Fig. S9,† the surface energies decrease slightly with the surface Ru/Co ratio from 1/168 to 1/48, while they decrease sharply when the surface Ru/Co ratio is lower than 1/24. In addition, the relative stability of each surface can be altered by different Ru coverage. When the Ru/Co ratio increases to 1/12, the Co(110) surface is even more stable than the Co(111) surface. The results reflected that Ru promoter plays an important role in tuning the stability of these Co surfaces.

The addition of Ru plays an important role in the modification of surface stability, and the change of stability of the exposed facets would further affect the morphology of FCC Co NPs. The Wulff shape of FCC Co NPs with different Ru content was constructed by minimizing the total surface energy, and the contribution of crystal facets to the total

Table 3 Surface energies (eV $Å^{-2}$) of Co surfaces modified by Ru at different Ru/Co atomic ratios

| | $\gamma^0_{Co(hkl)}$ | $\gamma^{ads}_{Co(hkl)}$ with Ru/Co ratio | | | | | |
|---|---|---|---|---|---|---|---|
| Surface | 0 | 1/168 | 1/120 | 1/96 | 1/48 | 1/24 | 1/12 |
| Co(111) | 0.132 | 0.126 | 0.124 | 0.122 | 0.111 | 0.090 | 0.048 |
| Co(100) | 0.158 | 0.153 | 0.150 | 0.148 | 0.139 | 0.120 | 0.082 |
| Co(311) | 0.161 | 0.154 | 0.151 | 0.149 | 0.137 | 0.112 | 0.063 |
| Co(110) | 0.157 | 0.150 | 0.146 | 0.144 | 0.129 | 0.100 | 0.042 |

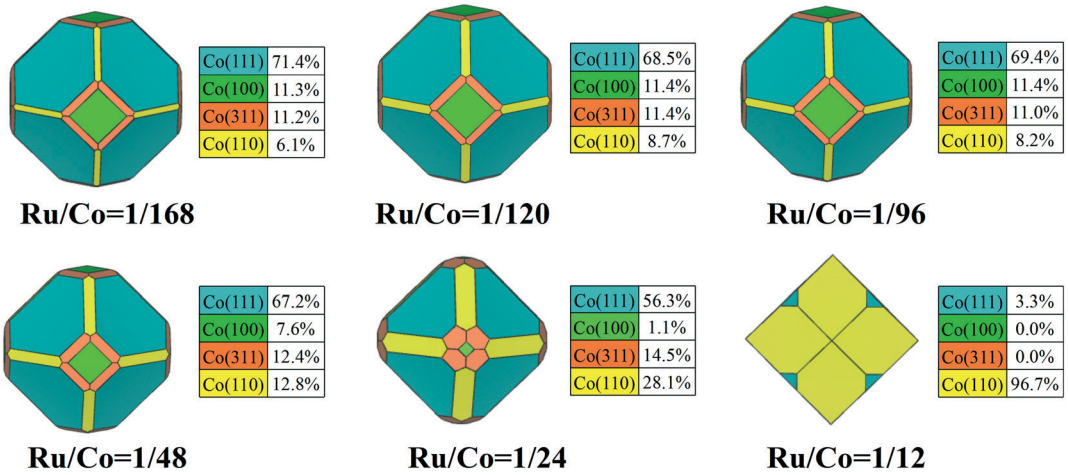


**Fig. 5** The equilibrium shapes of FCC Co modified using different Ru content values, and the fraction of each facet.



surface area was also determined to quantify the morphological changes. To clearly visualize the morphology evolution of FCC Co NPs induced by Ru promoter, all the constructed Wulff shapes are summarized and organized in Video S3.† As shown in Fig. 5, the crystallite morphology changed slightly with Ru/Co ratio from 1/168 to 1/24, showing an octahedron-like shape similar to the structure of pure FCC Co NPs. With Ru/Co up to 1/12, the corresponding morphology of the FCC Co NPs is a rhombic dodecahedron composed of Co(111) and Co(110) facets, apparently distinct from that with low Ru content.

With the increase of Ru/Co ratio, Co(311) and Co(110) facets are predicted to expose more area at the cost of the proportion of the Co(111) and Co(100) facets decreasing. Until the Ru/Co ratio is 1/24, Co(111) remains the predominately exposed surface of FCC Co, accounting for 56.3% of the total surface area because of its high stability. As the Ru/Co ratio continues to increase, the overall contribution from flat facets decreases in the equilibrium morphology, while the corrugated facets show a considerable surface area. This reveals that the morphology of the FCC Co nanoparticles is predominately dictated by the (111) and (110) facets once the Ru/Co ratio reaches 1/12. Obviously, Ru adsorption leads to dramatic changes in the surface morphology and the exposed facets of the Co nanocrystals, and high Ru content can help to facilitate the exposure of the high Miller index surfaces.

The existence of Ru promoter leads to the change in surface morphology and the relative ratios of exposed facets, which may affect the intrinsic activity and selectivity of the Co catalyst. It is reported that the Co(111) surface has a very low reactivity towards direct CO dissociation, with an activation energy barrier of 2.48 eV.[63] However, the $C_2$ hydrocarbon formation could be facilitated and the $CH_4$ formation could be suppressed by the stepped-Co(111) surface, owing to the step sites involved.[64] For the Co(100) surface, the calculated barrier (1.52 eV) for the H-assisted route is comparable to the direct route and also much higher than what is typically expected from FTS experiments.[65–67] In addition, the CO dissociation at step and kink sites is predicted to have the highest relative rate of all adsorption site types exposed on FCC Co NPs, these active sites generally exposed in the high index Co(311) and Co(110) surfaces are mainly responsible for the activity of the Co catalyst.[68] What is clear from our results is that the overall contribution from corrugated Co(311) and/or Co(110) surfaces increases in the equilibrium morphology with increasing Ru content, concurrently occurring with increment of step $B_5$ sites as well as kink 5F sites. These step and kink sites are more facile for CO dissociation on FCC Co NPs,[47] owing to the lower activation energy, as also concluded for Ru NPs.[69] The more active sites with higher intrinsic activity participating in the reaction could effectively enhance the catalytic activity of the Co catalyst. The results revealed that the high index facets stabilized by the increased Ru content would exhibit high activity for CO activation, which is valuable for developing more efficient and stable Co catalysts with higher reactivity for FTS reactions.

## 4. Conclusions

Combining density functional theory and *ab initio* molecular dynamic simulations, the adsorption configurations and growth trends of $Ru_n$ clusters on FCC Co surfaces in Fischer–Tropsch catalysis were investigated in order to clarify the facet-dependent equilibrium morphology of metallic Co NPs stabilized by Ru promoter. It is found that the difference in the adsorption patterns of $Ru_n$ clusters on Co surfaces arises from their distinct surface structures as well as Co–Ru interactions. The aggregation properties leading to the planar growth of $Ru_n$ clusters from the DFT calculations were demonstrated by the AIMD results, indicating that it is possible to predict accurately the growth process of Ru promoter on FCC Co catalysts. In addition, the Ru promoter shows different stabilization abilities on the exposed facets of the FCC Co NPs and has great influence on the

crystallographic morphology. Increased Ru content can facilitate the formation of high index active facets at large percentages; for example, Co(311) and Co(110) surfaces are predicted to expose more area, instead of Co(111) and Co(100) surfaces, meaning that more active sites with higher intrinsic activity participate in the reaction. As far as we know, this work is the first attempt to explore the surface morphology of FCC Co induced by Ru in a systematic way, which will help to design desired FTS catalysts rationally with high performance.

## Conflicts of interest

There are no conflicts to declare.

## Acknowledgements

The work was supported by the National Natural Science Foundation of China (Grant No. 21736007, 21872162, 21703273), the "Transformational Technologies for Clean Energy and Demonstration", the Strategic Priority Research Program of the Chinese Academy of Sciences (No. XDA 21020202) and the ShanXi Provincial Research Foundation for Basic Research (No. 201701D221242). The authors are grateful to Lvliang's cloud computing center for computational resources by the Tianhe-2.

## References

1 F. Jiao, J. Li, X. Pan, J. Xiao, H. Li, H. Ma, M. Wei, Y. Pan, Z. Zhou and M. Li, *Science*, 2016, **351**, 1065–1068.
2 J. Li, Y. He, L. Tan, P. Zhang, X. Peng, A. Oruganti, G. Yang, H. Abe, Y. Wang and N. Tsubaki, *Nat. Catal.*, 2018, **1**, 787–793.
3 A. J. Markvoort, R. A. van Santen, P. A. Hilbers and E. J. Hensen, *Angew. Chem., Int. Ed.*, 2012, **51**, 9015–9019.
4 X. Peng, K. Cheng, J. Kang, B. Gu, X. Yu, Q. Zhang and Y. Wang, *Angew. Chem., Int. Ed.*, 2015, **54**, 4553–4556.
5 Z. P. Liu and P. Hu, *J. Am. Chem. Soc.*, 2002, **124**, 11568–11569.
6 Q. Zhang, J. Kang and Y. Wang, *ChemCatChem*, 2010, **2**, 1030–1058.
7 R. Zhang, G. Wen, H. Adidharma, A. G. Russell, B. Wang, M. Radosz and M. Fan, *ACS Catal.*, 2017, **7**, 8285–8295.
8 H. M. T. Galvis, J. H. Bitter, C. B. Khare, M. Ruitenbeek, A. I. Dugulan and K. P. de Jong, *Science*, 2012, **335**, 835–838.
9 I. K. van Ravenhorst, C. Vogt, H. Oosterbeek, K. W. Bossers, J. G. Moya-Cancino, A. P. van Bavel, A. M. J. van der Eerden, D. Vine, F. M. F. de Groot, F. Meirer and B. M. Weckhuysen, *Angew. Chem., Int. Ed.*, 2018, **57**, 11957–11962.
10 I. A. Filot, R. A. van Santen and E. J. Hensen, *Angew. Chem., Int. Ed.*, 2014, **53**, 12746–12750.
11 G. Wen, Q. Wang, R. Zhang, D. Li and B. Wang, *Phys. Chem. Chem. Phys.*, 2016, **18**, 27272–27283.
12 C. Qin, B. Hou, J. Wang, Q. Wang, G. Wang, M. Yu, C. Chen, L. Jia and D. Li, *ACS Catal.*, 2018, **8**, 9447–9455.
13 H. Liu, R. Zhang, L. Ling, Q. Wang, B. Wang and D. Li, *Catal. Sci. Technol.*, 2017, **7**, 3758–3776.
14 P. Senecal, S. D. M. Jacques, M. Di Michiel, S. A. J. Kimber, A. Vamvakeros, Y. Odarchenko, I. Lezcano-Gonzalez, J. Paterson, E. Ferguson and A. M. Beale, *ACS Catal.*, 2017, **7**, 2284–2293.
15 G. Prieto, M. I. S. De Mello, P. Concepción, R. Murciano, S. B. C. Pergher and A. N. Martínez, *ACS Catal.*, 2015, **5**, 3323–3335.
16 Y. Liu, B. de Tymowski, F. Vigneron, I. Florea, O. Ersen, C. Meny, P. Nguyen, C. Pham, F. Luck and C. Pham-Huu, *ACS Catal.*, 2013, **3**, 393–404.
17 G. R. Johnson and A. T. Bell, *ACS Catal.*, 2016, **6**, 100–114.
18 S. Kattel, W. Yu, X. Yang, B. Yan, Y. Huang, W. Wan, P. Liu and J. G. Chen, *Angew. Chem., Int. Ed.*, 2016, **55**, 7968–7973.
19 H. Wang, W. Zhou, J. X. Liu, R. Si, G. Sun, M. Q. Zhong, H. Y. Su, H. B. Zhao, J. A. Rodriguez, S. J. Pennycook, J. C. Idrobo, W. X. Li, Y. Kou and D. Ma, *J. Am. Chem. Soc.*, 2013, **135**, 4149–4158.
20 K. M. Cook, H. D. Perez, C. H. Bartholomew and W. C. Hecker, *Appl. Catal., A*, 2014, **482**, 275–286.
21 O. Kungurova, N. Shtertser, G. Chermashentseva, I. Simentsova and A. Khassin, *Catalysis in Industry*, 2017, **9**, 23–30.
22 T. N. Phaahlamohlaka, D. O. Kumi, M. W. Dlamini, R. Forbes, L. L. Jewell, D. G. Billing and N. J. Coville, *ACS Catal.*, 2017, **7**, 1568–1578.
23 C. J. Weststrate, A. M. Saib and J. W. Niemantsverdriet, *Catal. Today*, 2013, **215**, 2–7.
24 N. Balakrishnan, B. Joseph and V. R. Bhethanabotla, *Appl. Catal., A*, 2013, **462–463**, 107–115.
25 R. Phienluphon, L. Shi, J. Sun, W. Niu, P. Lu, P. Zhu, T. Vitidsant, Y. Yoneyama, Q. Chen and N. Tsubaki, *Catal. Sci. Technol.*, 2014, **4**, 3099–3107.
26 M. J. Parnian, A. Taheri Najafabadi, Y. Mortazavi, A. A. Khodadadi and I. Nazzari, *Appl. Surf. Sci.*, 2014, **313**, 183–195.
27 N. Tsubaki, S. Sun and K. Fujimoto, *J. Catal.*, 2001, **199**, 236–246.
28 C. Pirola, M. Scavini, F. Galli, S. Vitali, A. Comazzi, F. Manenti and P. Ghigna, *Fuel*, 2014, **132**, 62–70.
29 T. Jermwongratanachai, G. Jacobs, W. Ma, W. D. Shafer, M. K. Gnanamani, P. Gao, B. Kitiyanan, B. H. Davis, J. L. S. Klettlinger, C. H. Yen, D. C. Cronauer, A. J. Kropf and C. L. Marshall, *Appl. Catal., A*, 2013, **464–465**, 165–180.
30 W. Ma, G. Jacobs, R. A. Keogh, D. B. Bukur and B. H. Davis, *Appl. Catal., A*, 2012, **437–438**, 1–9.
31 E. Iglesia, S. L. Soled, R. A. Fiato and G. H. Via, *J. Catal.*, 1993, **143**, 345–368.
32 E. Iglesia, S. L. Soled, R. A. Fiato and G. H. Via, *Dispersion, support, and bimetallic effects in Fischer-Tropsch synthesis on cobalt catalysts/Studies in Surface Science and Catalysis*, 1994, vol. 81, pp. 433–442.
33 O. A. Kungurova, A. A. Khassin, S. V. Cherepanova, A. A. Saraev, V. V. Kaichev, N. V. Shtertser, G. K. Chermashentseva, E. Y. Gerasimov, E. A. Paukshtis, O. V. Vodyankina, T. P. Minyukova and G. Abou-Jaoude, *Appl. Catal., A*, 2017, **539**, 48–58.

 

34 J. Hong, E. Marceau, A. Y. Khodakov, L. Gaberová, A. Griboval-Constant, J.-S. Girardon, C. L. Fontaine and V. Briois, *ACS Catal.*, 2015, **5**, 1273–1282.
35 M. Shannon, C. Lok and J. Casci, *J. Catal.*, 2007, **249**, 41–51.
36 M. Duan, J. Yu, J. Meng, B. Zhu, Y. Wang and Y. Gao, *Angew. Chem., Int. Ed.*, 2018, **57**, 6464–6469.
37 W. Piskorz, J. Gryboś, F. Zasada, P. Zapała, S. Cristol, J.-F. Paul and Z. Sojka, *J. Phys. Chem. C*, 2012, **116**, 19307–19320.
38 C.-F. Huo, B.-S. Wu, P. Gao, Y. Yang, Y.-W. Li and H. Jiao, *Angew. Chem., Int. Ed.*, 2011, **50**, 7403–7406.
39 S. Zhao, X.-W. Liu, C.-F. Huo, X.-D. Wen, W. Guo, D. Cao, Y. Yang, Y.-W. Li, J. Wang and H. Jiao, *Catal. Today*, 2016, **261**, 93–100.
40 Q. Li, M. Rellan-Pineiro, N. Almora-Barrios, M. Garcia-Rates, I. N. Remediakis and N. Lopez, *Nanoscale*, 2017, **9**, 13089–13094.
41 L. Liu, M. Yu, B. Hou, Q. Wang, B. Zhu, L. Jia and D. Li, *Nanoscale*, 2019, **11**, 8037–8046.
42 J. Meng, B. E. Zhu and Y. Gao, *J. Phys. Chem. C*, 2018, **122**, 6144–6150.
43 T. N. Phaahlamohlaka, M. W. Dlamini, M. W. Mogodi, D. O. Kumi, L. L. Jewell, D. G. Billing and N. J. Coville, *Appl. Catal., A*, 2018, **552**, 129–137.
44 L. Liu, M. Yu, Q. Wang, B. Hou, Y. Liu, Y. Wu, Y. Yang and D. Li, *Catal. Sci. Technol.*, 2018, **8**, 2728–2739.
45 N. Ashcroft and N. Mermin, *Solid State Physics*, Thomson Learning/Inc., Florence, 1976, p. 404.
46 J. Swart, E. Van Steen, I. Ciobîcă and R. Van Santen, *Phys. Chem. Chem. Phys.*, 2009, **11**, 803–807.
47 M. A. Petersen, J.-A. van den Berg, I. M. Ciobica and P. van Helden, *ACS Catal.*, 2017, **7**, 1984–1992.
48 H. J. Monkhorst and J. D. Pack, *Phys. Rev. B: Solid State*, 1976, **13**, 5188.
49 G. Kresse and J. Hafner, *Phys. Rev. B: Condens. Matter Mater. Phys.*, 1993, **47**, 558.
50 G. Kresse and J. Furthmüller, *Phys. Rev. B: Condens. Matter Mater. Phys.*, 1996, **54**, 11169.
51 J. P. Perdew, K. Burke and M. Ernzerhof, *Phys. Rev. Lett.*, 1996, **77**, 3865.
52 P. E. Blöchl, *Phys. Rev. B: Condens. Matter Mater. Phys.*, 1994, **50**, 17953.
53 G. Kresse and D. Joubert, *Phys. Rev. B: Condens. Matter Mater. Phys.*, 1999, **59**, 1758.
54 R. Bader, *International Series of Monographs on Chemistry*, 1990, vol. 22, pp. 9–15.
55 G. Henkelman, A. Arnaldsson and H. Jónsson, *Comput. Mater. Sci.*, 2006, **36**, 354–360.
56 G. Henkelman, B. P. Uberuaga and H. Jónsson, *J. Chem. Phys.*, 2000, **113**, 9901–9904.
57 P. Li, J. Liu, N. Nag and P. Crozier, *Appl. Catal., A*, 2006, **307**, 212–221.
58 G. R. Johnson and A. T. Bell, *J. Catal.*, 2016, **338**, 250–264.
59 M. Wang, S. Guo, Z. Li, Z. Ma, J. Wang, B. Hou, L. Jia and D. Li, *Fuel*, 2019, **241**, 669–675.
60 Y. Yang, L. Jia, B. Hou, D. Li, J. Wang and Y. Sun, *J. Phys. Chem. C*, 2014, **118**, 268–277.
61 Y. Yang, L. Jia, B. Hou, D. Li, J. Wang and Y. Sun, *Catal. Sci. Technol.*, 2014, **4**, 717–728.
62 S. Li, H. Li, J. Liu, X. Xue, Y. Tian, H. He and Y. Jia, *Phys. Rev. B: Condens. Matter Mater. Phys.*, 2007, **76**, 045410.
63 J.-X. Liu, H.-Y. Su, D.-P. Sun, B.-Y. Zhang and W.-X. Li, *J. Am. Chem. Soc.*, 2013, **135**, 16284–16287.
64 C. Chen, Q. Wang, G. Wang, B. Hou, L. Jia and D. Li, *J. Phys. Chem. C*, 2016, **120**, 9132–9147.
65 P. van Helden, I. M. Ciobîcă and R. L. Coetzer, *Catal. Today*, 2016, **261**, 48–59.
66 Z.-J. Wang, Z. Yan, C.-J. Liu and D. W. Goodman, *ChemCatChem*, 2011, **3**, 551–559.
67 C. G. Cooper, T.-H. Nguyen, Y.-J. Lee, K. M. Hardiman, T. Safinski, F. P. Lucien and A. A. Adesina, *Catal. Today*, 2008, **131**, 255–261.
68 W. Chen, T. Lin, Y. Dai, Y. An, F. Yu, L. Zhong, S. Li and Y. Sun, *Catal. Today*, 2018, **311**, 8–22.
69 H. Li, G. Fu and X. Xu, *Phys. Chem. Chem. Phys.*, 2012, **14**, 16686–16694.